Journal of Fluids and Structures (2001) **15,** 1187–1205
doi:10.1006/jfls.2001.0395, available online at http://www.idealibrary.com on IDEAL®

UNSTEADY CONFINED VISCOUS FLOWS WITH OSCILLATING WALLS AND MULTIPLE SEPARATION REGIONS OVER A DOWNSTREAM-FACING STEP

D. Mateescu and D. A. Venditti

Department of Mechanical Engineering, McGill University
Montreal, Quebec, Canada H3A 2K6

(Received 1 November 2000, and in final form 7 February 2001)

This paper presents computational solutions for unsteady viscous flows in channels with a downstream-facing step, followed by an oscillating floor. These solutions of the unsteady Navier–Stokes equations are obtained with a *time-integration method* using *artificial compressibility* in a *fixed* computational domain, which is obtained via a *time-dependent coordinate transformation* from the fluid domain with moving boundaries. The computational method is first validated for steady viscous flows past a downstream-facing step by comparison with previous numerical solutions and experimental results. This method is then used to obtain solutions for unsteady viscous flows with multiple separation regions over a downstream-facing step with oscillating walls, for which there are no previously known solutions. Thus, the present results may be used as benchmark solutions for the unsteady viscous flows with multiple separation regions between fixed and oscillating walls.

1. INTRODUCTION

The analysis of unsteady confined flows with oscillating boundaries has recently received an increased research interest for its applications to numerous engineering problems. The unsteady annular flows between cylindrical structures executing transverse oscillations, which are of particular interest for flow-induced vibration problems encountered in many engineering systems, have been studied theoretically (based on simplified theoretical models) and experimentally by numerous scientists, such as Chen *et al.* (1976), Inada & Hayama (1990), Mateescu & Païdoussis (1985, 1987), Mateescu *et al.* (1988, 1989) and others. These simplified theoretical models were proven to be in good agreement with experimental results, at least for simple cylindrical geometries (Mateescu *et al.* 1989).

For more realistic and complex geometric configurations, there was a need for more accurate solutions based on the time-accurate integration of the Navier–Stokes equations. The computational methods developed for this purpose should display a high degree of accuracy and computational efficiency in order to eventually permit the *simultaneous time integration of the Navier–Stokes equations and the structural equations of motion*, which is required in the study of the fluid–structure interactions. Several such computational methods have recently been developed based on a *time-integration formulation* with *artificial compressibility* (Mateescu *et al.* 1994a,b, 1996) and on *spectral-collocation* or *hybrid-spectral formulations* (Mateescu *et al.* 1994c, 1995), for the analysis of unsteady viscous flows with oscillating boundaries.

The unsteady confined flows with oscillating walls encountered in many engineering applications often display regions of separated flows, generated by sharp geometric changes of the fixed or oscillating walls. The correct numerical solution of these recirculating flow

0889–9746/01/081187 + 19 $35.00/0

regions in the presence of oscillating walls is essential in order to obtain correct numerical solutions for the overall unsteady flow. For this reason there is a need for benchmark solutions of unsteady viscous flows with separation regions in the presence of oscillating boundaries in order to validate the numerical methods developed for this purpose.

For steady viscous flows with multiple separation regions, the two-dimensional viscous flow over a downstream-facing step represents a benchmark problem, which was extensively used to validate the computational solutions by comparing them with previous numerical or experimental results. The importance of such flows with separation regions has been underlined by numerous authors, such as Abbott & Kline (1962) and Goldstein *et al.* (1970). Numerical solutions and experimental results were obtained by, among others, Armaly *et al.* (1983), Goldstein *et al.* (1970), Gartling (1990), Kim & Moin (1985), Lee & Mateescu (1998), and Sohn (1988). The locations of the separation and reattachment points of the recirculation regions, evaluated numerically and measured experimentally, were used as criteria for the validation of the numerical methods and the experimental techniques.

However, for the unsteady viscous flows with separation regions and oscillating walls past downstream-facing steps there are no previously known numerical solutions or experimental results. Hence, the unsteady flow solutions obtained in this paper for channels with downstream-facing steps can be considered benchmark solutions for unsteady viscous flows with multiple separation regions in the presence of oscillating walls.

A numerical method is first developed in this paper for the analysis of unsteady confined flows with oscillating walls, based on the accurate time integration of the Navier–Stokes equations. This time-integration method, using artificial compressibility, is applied in a *fixed* computational domain obtained via a *time-dependent coordinate transformation* from the real fluid flow domain with oscillating boundaries. The main features of the numerical method are presented in Section 3.

This numerical method is first validated for steady flows past a downstream-facing step, by extensive comparisons with previous numerical solutions and experimental results. Then, this time-integration method is used to obtain, for the first time, the solution for the benchmark problem of unsteady viscous flows in channels with downstream-facing steps and oscillating walls, for which no previous solutions are known.

2. PROBLEM FORMULATION

The geometry of the two-dimensional channel flow over a downstream-facing step is shown in Figure 1. It consists in an upstream channel of height h followed by a suddenly enlarged channel of height H. The channel lengths of the portions situated upstream and downstream of the backstep are l_0H and l_1H, respectively. In the numerical calculations presented in this paper, the downstream channel height was taken as being twice the

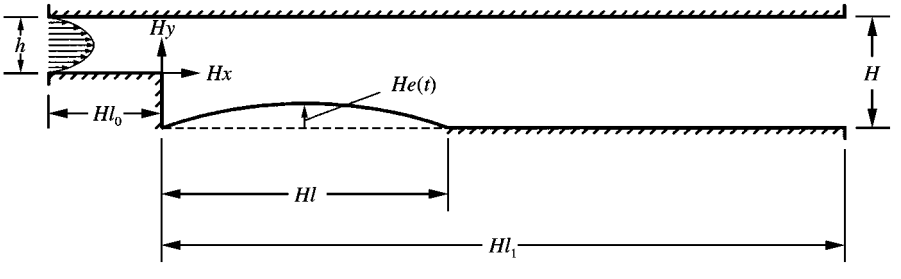

Figure 1. Geometry of the unsteady flow channel with a downstream-facing step followed by an oscillating floor of length Hl.

upstream portion of the channel, $H = 2\,h$, and hence the height of the downstream-facing step was equal to the upstream channel height, $h_s = h = \frac{1}{2}H$. This geometry was used for an easy comparison with previous numerical and experimental results for steady flows, which were mostly obtained for these geometrical parameters.

The flow is referred to the Cartesian coordinates, Hx and Hy, centred at the step corner, where x and y are nondimensional coordinates with respect to the downstream height, H. At the upstream end of the channel there is a fully developed laminar flow defined by the steady axial velocity

$$U(y) = 24\,U_0\,y(0{\cdot}5 - y), \quad \text{for } x = -l_0 \text{ and } y \in [0,\, 0{\cdot}5], \tag{1}$$

where U_0 represents the mean axial flow velocity.

In the steady flow analysis discussed for the method validation in Section 4, in addition to the above upstream flow condition corresponding to the physical flow problem (with the nondimensional upstream length, l_0, taken in the range 0·5–2 in the present computations), another case of upstream boundary condition is also considered for comparison with Gartling's benchmark solution (1990). In this case, the upstream length of the channel is taken to be zero ($l_0 = 0$), and the fully developed laminar velocity profile (1) is assumed just above the downstream-facing step at the entrance of the downstream channel.

In the unsteady flow case, a portion of the lower wall of length Hl, situated just behind the downstream-facing step, is assumed to execute transverse oscillations defined by the following lower wall equation:

$$Hy = \begin{cases} Hg(x,t) - h_s & \text{for } x \in [0, l], \\ -h_s & \text{for } x > l, \end{cases} \tag{2}$$

where $g(x, t)$ is a sinusoidal-shape mode defined as

$$g(x,t) = e(t)\sin(\pi x/l), \quad \text{where} \quad e(t) = A\cos(\omega t), \tag{3}$$

in which $t = U_0 t^*/H$ and $\omega = \omega^* H/U_0$ represent the nondimensional time and reduced frequency of oscillation (where $\omega^* = 2\pi f$ is the radian frequency of oscillation), respectively, and A is the nondimensional oscillation amplitude (nondimensionalized with respect to H).

No-slip boundary conditions are implemented at the solid walls. The inflow and outflow boundaries of the computational domain are situated at a distance Hl_0 and Hl_1 upstream and downstream from the step, respectively, with $l_0 = 2$ and $l_1 = 30$ in the present computations. The outflow boundary conditions for the velocity components are based on an extrapolation to second-order accuracy from inside the computational domain. The outlet pressure is obtained by integrating the normal momentum equation from the bottom wall (Mateescu *et al.* 1994a), and in the final solution the pressure is adjusted to zero at the concave step corner.

The incompressible time-dependent Navier–Stokes and continuity equations can be expressed in nondimensional conservation law form as

$$\frac{\partial \mathbf{V}}{\partial t} + \mathbf{Q}(\mathbf{V}, p) = \mathbf{0}, \quad \nabla \cdot \mathbf{V} = 0, \tag{4}$$

where $\mathbf{V}$, which represents the dimensionless fluid velocity vector, is nondimensionalized with respect to U_0, and $\mathbf{Q}(\mathbf{V}, p)$, which includes the convective derivative, pressure and viscous terms, can be expressed in two-dimensional Cartesian coordinates in the form

$$\mathbf{V} = \{u, v\}^{\mathrm{T}}, \quad \mathbf{Q}(\mathbf{V}, p) = \{Q_u(u,\, v,\, p),\, Q_v(u,\, v,\, p)\}^{\mathrm{T}}, \tag{5}$$

$$Q_u(u, v, p) = \frac{\partial(uu)}{\partial x} + \frac{\partial(vu)}{\partial y} + \frac{\partial p}{\partial x} - \frac{1}{\mathrm{Re}}\left(\frac{\partial^2 u}{\partial x^2} + \frac{\partial^2 u}{\partial y^2}\right), \tag{6}$$

$$Q_v(u, v, p) = \frac{\partial(uv)}{\partial x} + \frac{\partial(vv)}{\partial y} + \frac{\partial p}{\partial y} - \frac{1}{\mathrm{Re}}\left(\frac{\partial^2 v}{\partial x^2} + \frac{\partial^2 v}{\partial y^2}\right), \tag{7}$$

$$\mathbf{V}\cdot\mathbf{V} = \frac{\partial u}{\partial x} + \frac{\partial v}{\partial y}, \tag{8}$$

in which $\mathrm{Re} = HU_0/v$ represents the Reynolds number based on the downstream channel height, and u, v and p represent the dimensionless velocity components and pressure, nondimensionalized with respect to U_0 and $\rho {U_0}^2$, respectively.

3. METHOD OF SOLUTION

For a rigorous implementation of the boundary conditions on the oscillating walls, the real fluid flow domain with moving boundaries is transformed into a fixed computational domain by the time-dependent coordinate transformation

$$X = x, \qquad Y = f(x, y, t), \qquad t = t, \tag{9}$$

where $f(x, y, t)$ is defined in terms of the oscillation mode, $g(x, t)$, as

$$f(x, y, t) = 1 - \frac{1 - h_s/H - y}{1 - g(x, t)}. \tag{10}$$

In this fixed computational domain, the Navier–Stokes and continuity equations can be expressed in the form

$$\frac{\partial \mathbf{V}}{\partial t} + \mathbf{G}(\mathbf{V}, p) = \mathbf{0}, \quad \mathscr{D}\mathbf{V} = 0, \tag{11}$$

where

$$\mathbf{V} = \{u, v\}^{\mathrm{T}}, \quad \mathbf{G}(\mathbf{V}, p) = \{G_u(u, v, p),\ G_v(u, v, p)\}^{\mathrm{T}} \tag{12}$$

$$G_u(u, v, p) = \frac{\partial(uu)}{\partial X} + C_1\frac{\partial^2 u}{\partial X^2} + C_2\frac{\partial(uu)}{\partial Y} + C_3\frac{\partial(vu)}{\partial Y} + C_4\frac{\partial u}{\partial Y} + \frac{\partial p}{\partial X} + C_2\frac{\partial p}{\partial Y} + C_5\frac{\partial^2 u}{\partial Y^2} + C_6\frac{\partial^2 u}{\partial Y \partial X}, \tag{13}$$

$$G_v(u, v, p) = \frac{\partial(uv)}{\partial X} + C_1\frac{\partial^2 v}{\partial X^2} + C_2\frac{\partial(uv)}{\partial Y} + C_3\frac{\partial(vv)}{\partial Y} + C_4\frac{\partial v}{\partial Y} + C_3\frac{\partial p}{\partial Y} + C_5\frac{\partial^2 v}{\partial Y^2} + C_6\frac{\partial^2 v}{\partial Y \partial X}, \tag{14}$$

$$\mathscr{D}\mathbf{V} = \frac{\partial u}{\partial X} + C_2\frac{\partial u}{\partial Y} + C_3\frac{\partial v}{\partial Y}, \tag{15}$$

in which

$$C_1 = -\frac{1}{\mathrm{Re}}, \qquad C_2 = \frac{\partial f}{\partial X}, \qquad C_3 = \frac{\partial f}{\partial Y}, \tag{16}$$

$$C_4 = \frac{\partial f}{\partial t} - \frac{1}{\mathrm{Re}}\left(\frac{\partial^2 f}{\partial X^2} + \frac{\partial^2 f}{\partial Y^2}\right), \quad C_5 = -\frac{1}{\mathrm{Re}}\left[\left(\frac{\partial f}{\partial X}\right)^2 + \left(\frac{\partial f}{\partial Y}\right)^2\right],$$

$$C_6 = -\frac{2}{\mathrm{Re}}\frac{\partial f}{\partial X}. \tag{17}$$

In the present approach, the momentum equation is discretized in real time based on a second-order three-point-backward implicit scheme:

$$(\partial \mathbf{V}/\partial t)^{n+1} = (3\mathbf{V}^{n+1} - 4\mathbf{V}^n + \mathbf{V}^{n-1})/(2\,\Delta t), \tag{18}$$

where the superscripts n-1, n and $n+1$ indicate three consecutive time levels, and $\Delta t = t^{n+1} - t^n = t^n - t^{n-1}$ represents the time step. Thus, equations (11) can be expressed at the time level t^{n+1} in the form

$$\mathbf{V}^{n+1} + \alpha \mathbf{G}^{n+1} = \mathbf{F}^n, \qquad \mathscr{D}\,\mathbf{V}^{n+1} = \mathbf{0}, \tag{19}$$

where

$$\alpha = 2\,\Delta t/3, \quad \mathbf{G}^{n+1} = \mathbf{G}(\mathbf{V}^{n+1}, p^{n+1}),$$

and

$$\mathbf{F}^n = (4\mathbf{V}^n + \mathbf{V}^{n-1})/3.$$

An iterative pseudo-time relaxation procedure with artificial compressibility is then used in order to advance the solution of the semi-discretized equations from the real-time level t^n to t^{n+1} in the form

$$\partial \check{\mathbf{V}}/\partial \tau + \check{\mathbf{V}} + \alpha \check{\mathbf{G}} = \mathbf{F}^n, \qquad \delta(\partial \check{p}/\partial \tau) + \mathscr{D}\,\check{\mathbf{V}} = 0, \tag{20}$$

where $\check{\mathbf{V}}(\tau)$ and $\check{p}(\tau)$ denote the pseudo-functions corresponding to the variable velocity and pressure at pseudo-time τ, between the real-time levels t^n and t^{n+1}, and δ represents an artificially added compressibility [the optimum value for δ is determined based on the theory of characteristics—see Mateescu *et al.* (1994a,b)]. An implicit Euler scheme is then used to discretize equations (20) between the pseudo-time levels τ^v and $\tau^{v+1} = \tau^v + \Delta\tau$, and the resulting equations are expressed in terms of the pseudo-time variations $\Delta u = \check{u}^{v+1} - \check{u}^v$, $\Delta v = \check{v}^{v+1} - \check{v}^v$, $\Delta p = \check{p}^{v+1} - \check{p}^v$, in the matrix form

$$[\mathbf{I} + \alpha \Delta\tau(\mathbf{D}_X + \mathbf{D}_Y)]\,\Delta\mathbf{f} = \Delta\tau \mathbf{S}, \tag{21}$$

where $\Delta\mathbf{f} = [\Delta u, \Delta v, \Delta p]^{\mathrm{T}}$, $\alpha = 2\,\Delta t/3$, $\mathbf{I}$ is the identity matrix, and

$$\mathbf{D}_X = \begin{bmatrix} M + \dfrac{1}{\alpha} & 0 & \dfrac{\partial}{\partial X} \\ 0 & M & 0 \\ \dfrac{1}{\alpha\delta}\dfrac{\partial}{\partial X} & 0 & 0 \end{bmatrix}, \qquad \mathbf{D}_Y = \begin{bmatrix} N & 0 & C_2\dfrac{\partial}{\partial Y} \\ 0 & N + \dfrac{1}{\alpha} & C_3\dfrac{\partial}{\partial Y} \\ \dfrac{C_2}{\alpha\delta}\dfrac{\partial}{\partial Y} & \dfrac{C_3}{\alpha\delta}\dfrac{\partial}{\partial Y} & 0 \end{bmatrix}, \tag{22}$$

$$\mathbf{S} = \begin{Bmatrix} F_u^n - \check{u}^v - \alpha G_u^v \\ F_v^n - \check{v}^v - \alpha G_v^v \\ -(1/\delta)\ \mathscr{D}\check{\mathbf{V}}^v \end{Bmatrix}, \tag{23}$$

in which the differential operators M and N are defined as

$$M\phi = \frac{\partial(\check{u}^v\phi)}{\partial X} + C_1 \frac{\partial^2\phi}{\partial X^2}, \tag{24}$$

$$N\phi = C_2 \frac{\partial(\check{u}^v\phi)}{\partial Y} + C_3 \frac{\partial(\check{v}^v\phi)}{\partial Y} + C_4 \frac{\partial\phi}{\partial Y} + C_5 \frac{\partial^2\phi}{\partial Y^2} + C_6 \frac{\partial^2\phi}{\partial Y \partial X}. \tag{25}$$

A factored alternate direction implicit (ADI) scheme is used to separate equation (21) into two successive sweeps in x and y, defined by the equations

$$[\mathbf{I} + \alpha \Delta\tau\, \mathbf{D}_Y)]\ \Delta\mathbf{f}^* = \Delta\tau\mathbf{S}, \qquad [\mathbf{I} + \alpha\Delta\tau\, \mathbf{D}_X)]\ \Delta\mathbf{f} = \Delta\mathbf{f}^*, \tag{26}$$

where $\Delta\mathbf{f}^* = [\Delta u^*, \Delta v^*, \Delta p^*]^{\mathrm{T}}$ is a convenient intermediate variable vector.

These equations are further spatially discretized by central differencing on a stretched staggered grid, based on hyperbolic sine and hyperbolic tangent stretching functions in the x- and y-directions, respectively. A special decoupling procedure, based on the utilization of the continuity equation, is then used for each sweep to reduce the resulting systems of discretized equations to two sets of decoupled scalar tridiagonal equations [for details on the spatial discretization and the decoupling procedure see Mateescu *et al.* (1994a,b)].

4. METHOD VALIDATION FOR THE STEADY VISCOUS FLOW WITH SEPARATION REGIONS OVER A DOWNSTREAM-FACING STEP

Before using it for the analysis of unsteady flows, this method has been applied for validation to the study of steady two-dimensional flows over a downstream-facing step. For a meaningful comparison with the previous numerical and experimental results, computations have been performed for the value of the channel expansion ratio, $H/h = 2$ (the step height being in this case equal to the upstream channel height, $h_s = h = H/2$), and for various Reynolds numbers, including $\mathrm{Re} = 800$ which has been most commonly used in the previous theoretical and experimental investigations. A fully developed laminar flow defined by the parabolic velocity profile (1) is considered at the channel inlet. The following two cases of the channel inlet geometry have been considered, again for meaningful comparisons.

(i) Case in which the upstream portion of the channel is missing, that is $l_0 = 0$, and the fully developed velocity profile (1) is assumed just above the downstream-facing step, at the entrance of the downstream channel. This case is considered for comparison with the benchmark numerical solution given by Gartling (1990), as well as with other previous numerical solutions.

(ii) The physical case in which the fully developed velocity profile (1) is assumed at the inlet of the upstream portion of the channel having the nondimensional length l_0 with respect to the downstream channel height, H. Computations were performed for increasing values of l_0 (starting from 0) in order to study the effect of the upstream length of the channel on the numerical solution obtained. It was found that increasing this nondimensional length, l_0, above 2 did not further influence the numerical solution for the range of Reynolds numbers considered.

TABLE 1
Computed nondimensional lengths of separation on the lower and upper walls and the upper wall separation and reattachment positions compared with previous numerical and experimental results

	Lower wall	Upper wall		
	Length of separation L_l	Length of separation $L_u = x_r - x_s$	Separation position x_s	Reattachment position x_r
Computational solutions for Re = 800 and $H/h = 2$				
Present solution for $l_0 = 2$ (with upstream channel)	5·90	5·65	4·66	10·31
Present solution for $l_0 = 0$ (without upstream channel)	6·09	5·63	4·85	10·47
Gartling (1990) ($l_0 = 0$)	6·10	5·63	4·85	10·48
Sohn (1988) ($l_0 = 0$)	5·8	4·7	—	—
Kim & Moin (1985) ($l_0 = 0$)	6·0	5·75	—	—
Experimental results				
Lee & Mateescu (1998)*	6·45	5·1	5·15	10·25
Armaly *et al.* (1983)†	7·0	4·3	5·7	10·0

* For Re = 805 and $H/h = 2$.
† For Re = 805 and $H/h = 1{\cdot}94$.

Unless otherwise stated, the numerical results for steady flows presented in the following were obtained using a stretched staggered grid with 1001×201 grid points for each variable (that is, 2001×401 grid points in total) in the case $l_0 = 0$, and 1097×201 grid points in the case $l_0 = 2$. The mesh spacing in the x-direction was minimum at the step, $\Delta x_{\min} = 0{\cdot}0104$ (for the staggered grid), and maximum at the outlet boundary, $\Delta x_{\max} = 0{\cdot}0252$, while in the y-direction the minimum mesh spacing was at the walls and the step corner, $\Delta y_{\min} = 0{\cdot}00182$. Computations were performed for a nondimensional length of the downstream channel, $l_1 = 30$, with $\delta = 0{\cdot}8$ and $\Delta\tau = 0{\cdot}4$, and convergence was considered to have been reached when all of the r.m.s. residuals were less than 10^{-9}.

For Re = 800, the flow over the downstream-facing step is characterized by two separation regions, one at the lower wall just behind the step and the other at the upper wall. The present results for the nondimensional lengths of separation on the lower and upper walls, L_l and $L_u = x_r - x_s$, and for the locations of the separation and reattachment points on the upper wall, x_s and x_r, respectively, are compared in Table 1 with previous numerical and experimental results. One can notice good agreement with the previous numerical solutions obtained for the case $l_0 = 0$. The agreement with the benchmark solution obtained by Gartling (1990) is excellent, and this can also be seen from Table 2 in which the cross-channel velocity profiles are compared for two axial locations, $x = 7$ and 15.

The agreement with the experimental results was not as good for this Reynolds number. Thus, the experimental results obtained by Armaly *et al.* (1983), by using a laser-Doppler velocimetry technique, displayed differences of the order of 20% with respect to the theoretical results. More recently, Lee & Mateescu (1998) performed very thorough experimental investigations using a nonintrusive technique based on multi-element hot-film sensors glued on the wall surface. As shown in Table 1, their experimental results were much closer to the numerical predictions, although the agreement cannot be considered satisfactory for this Reynolds number.

As suggested by Armaly *et al.* (1983), Kim & Moin (1985) and Gartling (1990), these discrepancies between the experimental results and the numerical predictions are due to

TABLE 2
Computed cross-channel velocity profiles compared with Gartling's benchmark solution (for $\mathrm{Re} = 800$ and $l_0 = 0$)

	Present solution				Gartling 1990			
	$x = 7$		$x = 15$		$x = 7$		$x = 15$	
y	u	$100\ v$	u	$100\ v$	u	$100\ v$	u	$100\ v$
0·50	0·000	0·000	0·000	0·000	0·000	0·000	0·000	0·000
0·45	−0·038	−0·027	0·101	0·020	−0·038	−0·027	0·101	0·021
0·40	−0·049	−0·086	0·202	0·072	−0·049	−0·086	0·202	0·072
0·35	−0·032	−0·147	0·304	0·139	−0·032	−0·147	0·304	0·140
0·30	0·015	−0·192	0·408	0·206	0·015	−0·193	0·408	0·207
0·25	0·093	−0·221	0·512	0·259	0·092	−0·225	0·512	0·260
0·20	0·204	−0·260	0·613	0·286	0·204	−0·268	0·613	0·288
0·15	0·349	−0·349	0·705	0·281	0·349	−0·362	0·704	0·283
0·10	0·523	−0·525	0·780	0·243	0·522	−0·544	0·779	0·245
0·05	0·710	−0·797	0·831	0·177	0·709	−0·823	0·831	0·180
0·00	0·886	−1·133	0·853	0·093	0·885	−1·165	0·853	0·095
−0·05	1·025	−1·469	0·844	0·002	1·024	−1·507	0·844	0·003
−0·10	1·106	−1·737	0·804	−0·083	1·105	−1·778	0·804	−0·081
−0·15	1·118	−1·884	0·737	−0·149	1·118	−1·925	0·737	−0·147
−0·20	1·061	−1·877	0·648	−0·186	1·062	−1·917	0·649	−0·185
−0·25	0·947	−1·712	0·546	−0·192	0·948	−1·748	0·547	−0·191
−0·30	0·791	−1·404	0·437	−0·167	0·792	−1·423	0·438	−0·166
−0·35	0·612	−0·976	0·327	−0·120	0·613	−1·000	0·328	−0·119
−0·40	0·426	−0·488	0·217	−0·065	0·428	−0·504	0·218	−0·065
−0·45	0·231	−0·112	0·108	−0·019	0·232	−0·118	0·109	−0·019
−0·50	0·000	0·000	0·000	0·000	0·000	0·000	0·000	0·000

three-dimensional effects in the experimental channel flows (as compared to the rigorous two-dimensional computational solutions), which appear to become significant for $\mathrm{Re} > 600$. This explanation seems to be confirmed by a very good agreement between the present numerical solutions and the experimental results for lower Reynolds numbers, such as $\mathrm{Re} = 400$ and 600. This can be seen for the lower wall separation length in Table 3, as well as in Figure 2, which shows the variation with the Reynolds number of the separation and reattachment locations on both the upper and lower walls.

A graphical illustration of the computed cross-channel velocity profile at various axial locations along the computational domain ($-2 < x < 30$) is shown in Figure 3 for $\mathrm{Re} = 800$ and an expansion ratio $H/h = 2$. The streamline contours, illustrating the recirculation regions near the upper and lower walls, are also shown in the background in this figure.

The sensitivity of the numerical solution with the mesh refinement was thoroughly investigated in order to define an optimum grid that can also be used for the unsteady computations, which require a much larger amount of computational time. Table 4 shows the computed separation and reattachment locations on the lower and upper walls for various grids. One can notice that the solution obtained by using 351×71 grid points for each variable (or 701×141 grid points in total) is very close to the fully converged solution, which is practically obtained with 1001×201 grid points, and beyond this the numerical solution is not influenced by the grid refinement. As a result, all computations for steady flows have been performed on a mesh with 1001×201 grid points for each variable (or 2001×401 grid points in total), and for unsteady flows (which require a substantially

TABLE 3
Computed nondimensional length of separation on the lower wall, L_l, compared with previous numerical and experimental results for various Reynolds numbers

	Re = 400	Re = 600	Re = 800	Re = 1000	Re = 1200
Computational solutions for $H/h = 2$					
Kim & Moin (1985) ($l_0 = 0$)	4·3	5·3	6·0	—	—
Sohn (1988) ($l_0 = 0$)	4·1	5·2	5·8	—	—
Present solution for $l_0 = 0$ (without upstream channel)	4·32	5·37	6·09	6·71	7·29
Present solution for $l_0 = 2$ (with upstream channel)	4·12	5·17	5·90	6·53	7·11
Experimental results for * $H/h = 2$; † $H/h = 1·94$					
Lee & Mateescu (1998)*	4·1	5·21	6·45	7·4	8·4
Armaly *et al.* (1983)†	4·3	5·8	7·1	8·1	8·9

*,† The experimental Reynolds numbers were slightly different in some cases (see also Figure 2).

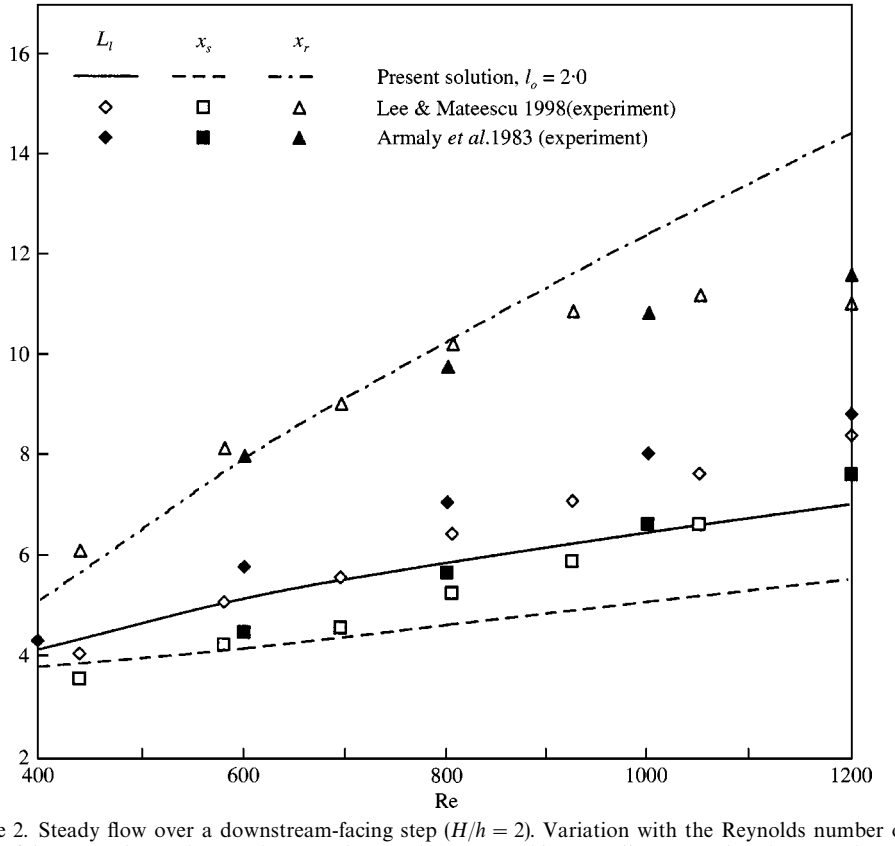

Figure 2. Steady flow over a downstream-facing step ($H/h = 2$). Variation with the Reynolds number of the location of the separation and reattachment points on the upper and lower walls. Comparison between the present theoretical solutions (—, lower wall reattachment; – – –, upper wall separation; –·–·–, upper wall reattachment) and experimental results: ◇, □, △, Lee & Mateescu (1998); ◆, ■, ▲, Armaly *et al.* (1983).

increased computational time) a mesh with 353×61 grid points for each variable (or 705×121 grid points in total) has been used instead.

The effect of the upstream length of the channel, l_0, has also been studied, and the results are shown in Table 5. One can notice that the solution obtained for $l_0 = 2$ is fully converged

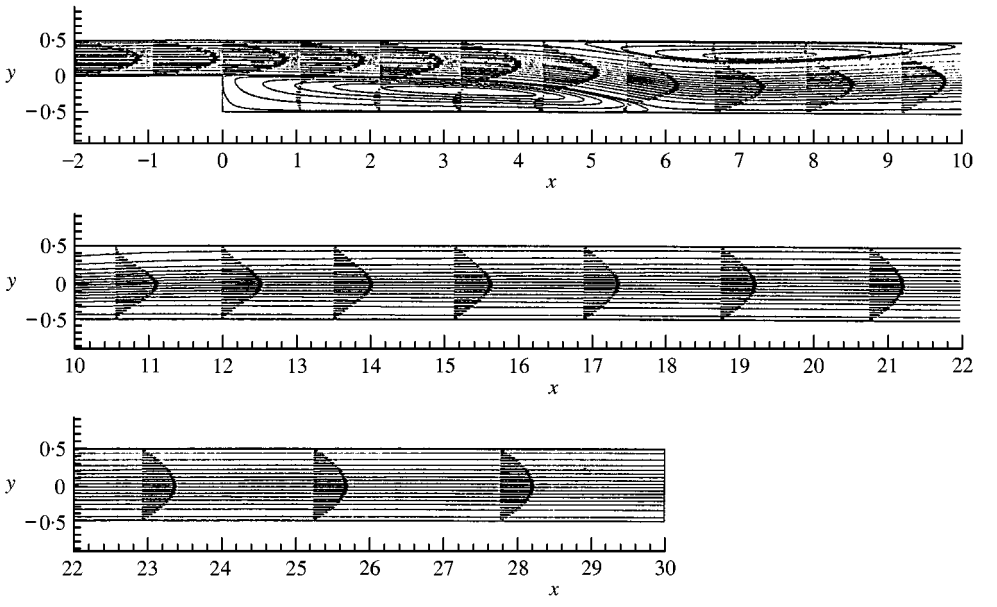

Figure 3. Steady flow over a downstream-facing step ($H/h = 2$ and $\mathrm{Re} = 800$). Typical cross-channel velocity profiles at various axial locations along the computational domain ($-2 < x < 30$), as well as the streamline contours illustrating the recirculation regions near the upper and lower walls.

TABLE 4
Grid sensitivity of the numerical solution for $H/h = 2$, $\mathrm{Re} = 800$ and $l_0 = 0$ based on the computed nondimensional lengths of separation and reattachment

	Lower wall	Upper wall		
Grid points used for each variable	L_l	$L_u = x_r - x_s$	x_s	x_r
201×41	5·92	5·66	4·67	10·33
251×51	5·99	5·65	4·74	10·39
301×61	6·02	5·65	4·77	10·44
351×71	6·04	5·64	4·80	10·42
401×81	6·05	5·64	4·81	10·45
501×101	6·07	5·63	4·83	10·46
601×121	6·08	5·63	4·83	10·47
801×161	6·09	5·63	4·84	10·47
1001×201	6·09	5·63	4·85	10·47
1201×241	6·09	5·63	4·85	10·48
1401×281	6·09	5·63	4·85	10·48

from this point of view, since an increase beyond this value did not further influence the numerical solution. For both the steady and unsteady flows the computations were performed for an upstream channel length $l_0 = 2$.

The location for the outflow boundary of the computational domain was taken at a nondimensional distance $l_1 = 30$ (based on the downstream height, H) behind the step, which corresponds to the value considered by Gartling (1990), and is double in comparison with the value used by Kim & Moin (1985). This distance, $l_1 = 30$, was proven to be adequate, since the cross-channel velocity profile settled to a parabolic shape well before the outflow boundary ($x = l_1 = 30$), as shown in Figure 3.

TABLE 5
Influence of the upstream channel length, Hl_0, on the numerical solution based on the computed nondimensional lengths of separation and reattachment for $H/h = 2$, Re = 800

		Lower wall	Upper wall		
Grid points used for each variable	l_0	L_l	$L_u = x_r - x_s$	x_s	x_r
1001×201	0·00	6·09	5·63	4·85	10·47
1025×201	0·50	5·95	5·60	4·71	10·31
1049×201	1·00	5·91	5·64	4·67	10·31
1073×201	1·50	5·90	5·65	4·66	10·31
1097×201	2·00	5·90	5·65	4·66	10·31

5. UNSTEADY VISCOUS FLOW WITH SEPARATIONS OVER A DOWNSTREAM-FACING STEP WITH OSCILLATING WALLS

After validation, this method has been used in the analysis of two-dimensional unsteady flows with multiple separation regions in ducts with a downstream-facing step and an oscillating floor behind the step, as illustrated in Figure 1. Computations have been performed for an expansion ratio $H/h = 2$ and for values of the Reynolds number, $\mathrm{Re} = HU_0/\nu$, ranging from 400 to 800, and of the oscillatory Reynolds number, $\beta = \omega^* H^2/\nu$, between 20 and 80, which corresponds to various values of the reduced frequency of oscillations, $\omega = \beta/\mathrm{Re}$, between 0·05 and 0·20. The length of the oscillating floor portion was $Hl = 10\,H$, and the upstream and downstream lengths of the computational domain are $l_0 = 2$ and $l_1 = 30$, respectively. A stretched staggered grid with 353×61 grid points for each variable (corresponding to 705×121 grid points in total) has been used for the unsteady flow computations.

The real-time step was obtained by dividing the period of oscillations by N, where $N = 40$ or 80 in some cases, which leads to a nondimensional value $\Delta t = 2\pi/(N\omega)$, where $\omega = \beta/\mathrm{Re}$. The pseudo-time computations have been performed using $\delta = 0{\cdot}25$ and $\Delta\tau = 0{\cdot}10$. It was found that an average number of 60 pseudo-time iterations per real-time step was required to reduce the r.m.s. residuals adequately until convergence (a maximum number of 150 pseudo-time iterations was required in some cases during the first oscillation cycle).

The real-time integration was started from the steady flow solution for fixed walls, and was performed until all variables in the computational domain were executing steady repeatable oscillations from one period to the next (usually after three oscillation cycles or less in the cases considered).

Unsteady flow computations have been performed for the case when a portion of the lower wall of length $Hl = 10\,H$ behind the step executes harmonic oscillations defined by equation (2) for several values of the amplitude of oscillations, A. The computed locations of the separation and reattachment points on the lower and upper walls are illustrated in Figures 4–6 for several values of the Reynolds number, $\mathrm{Re} = HU_0/\nu$, between Re = 400 and 800, for various values of the reduced frequency $\omega = \omega^* H/U_0$, in the range $\omega = 0{\cdot}05$ and 0·20 (which corresponds to an oscillatory Reynolds number, $\beta = \omega^* H^2/\nu$, between 20 and 80) and for several values of the nondimensional amplitude of oscillations, A, from $A = 0{\cdot}001$ to 0·1. The variation in time of the mid-point displacement of the lower oscillating wall is also indicated in Figures 4–6.

The influence of the Reynolds number on the location of the separation and reattachment points is shown in Figure 4 for $\omega = 0{\cdot}05$ and $A = 0{\cdot}05$. One can notice that the locations of

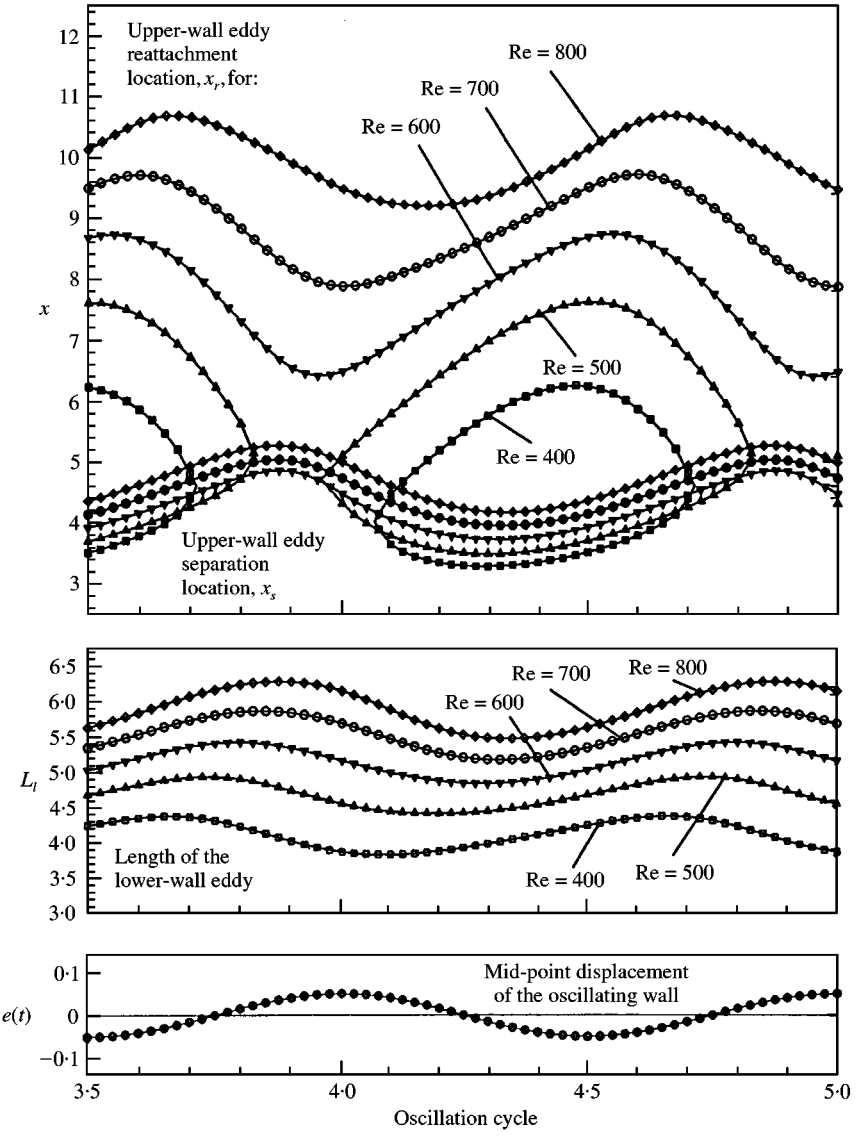

Figure 4. Unsteady flow over a downstream-facing step with an oscillating floor ($H/h = 2$). Typical influence of Reynolds number, Re, on the variation in time of the location of the separation and reattachment points on the upper and lower walls for $\omega = 0{\cdot}05$ and $A = 0{\cdot}05$.

the separation and reattachment points on the lower and upper walls computed for Re = 600, 700 and 800 display oscillations in time, but both separation regions are present during the entire oscillatory cycle.

However, it was found that for Re = 400 and 500 the upper recirculation region is present only during a certain portion of the oscillatory cycle, and simply disappears during the rest of the cycle, as shown in Figure 4 (the lower wall separation generated by the downstream-facing step is always present). Thus, for Re = 400 the upper separation region is absent for almost half of the oscillatory cycle.

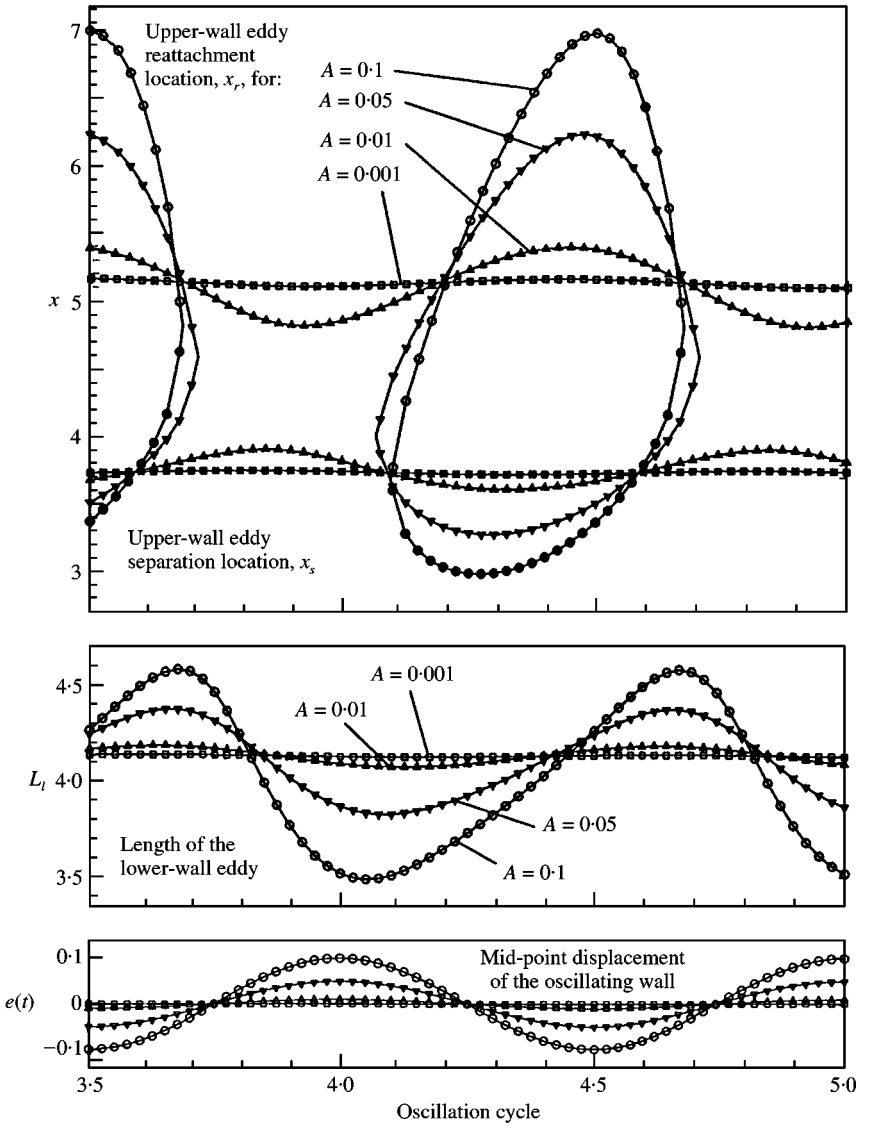

Figure 5. Unsteady flow over a downstream-facing step with an oscillating floor ($H/h = 2$). Typical influence of the amplitude of oscillations, A, on the variation in time of the location of the separation and reattachment points on the upper and lower walls for Re = 400 and $\omega = 0{\cdot}05$.

It was also found that the maximum length of the upper separation region (during an oscillation cycle) increases substantially with the Reynolds number, with more than a two-fold increase from Re = 400 to 800. This observation is also valid for the lower separation region, although the extent of increase is somewhat smaller.

The influence of the amplitude of oscillations, A, on the location of the separation and reattachment edges is shown in Figure 5 for Re = 400 and $\omega = 0{\cdot}05$. It was found that the upper separation region is continuously present in time in the case of small amplitude oscillations, such as $A = 0{\cdot}01$, but disappears for a good portion of the oscillation cycle in the case of larger amplitude, such as $A = 0{\cdot}05$ and $0{\cdot}01$. At the same time, the length of

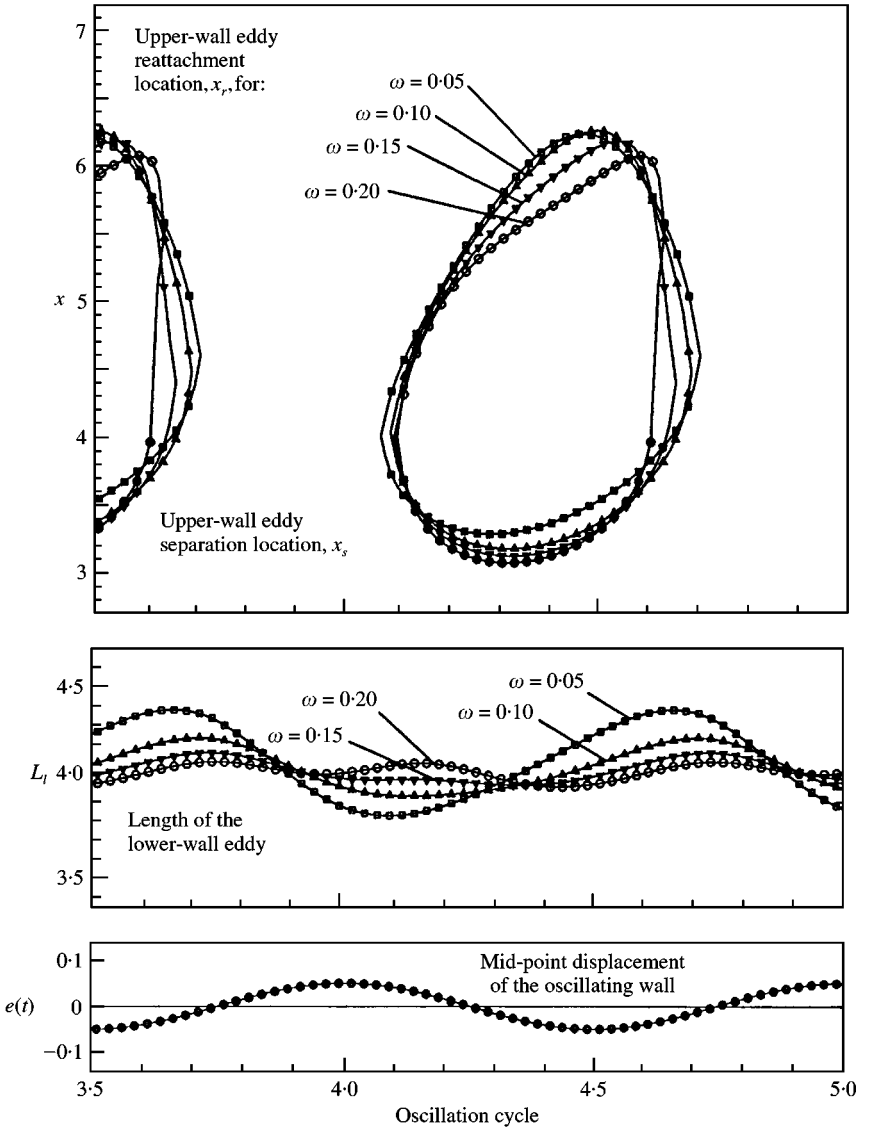

Figure 6. Unsteady flow over a downstream-facing step with an oscillating floor ($H/h = 2$). Typical influence of the reduced frequency of oscillations, ω, on the variation in time of the location of the separation and reattachment points on the upper and lower walls for Re = 400 and $A = 0{\cdot}05$.

the upper separation region increases substantially with the amplitude of oscillation, the maximum length becoming more than double at $A = 0{\cdot}1$ in comparison to $A = 0{\cdot}01$. The variation in time of the location of the lower wall reattachment also increases substantially with the amplitude of oscillations. Figure 5 also shows the location of the separation and reattachment points in the case of an extremely low amplitude oscillation of the wall, $A = 0{\cdot}001$, which practically coincides with the results obtained for the steady flow.

The influence of the reduced frequency of oscillations, ω (or that of the oscillatory Reynolds number, $\beta = \omega\,\mathrm{Re}$) on the location of the separation and reattachment points is shown in Figure 6 for Re = 400 and $A = 0{\cdot}05$; in this figure, the points representing the

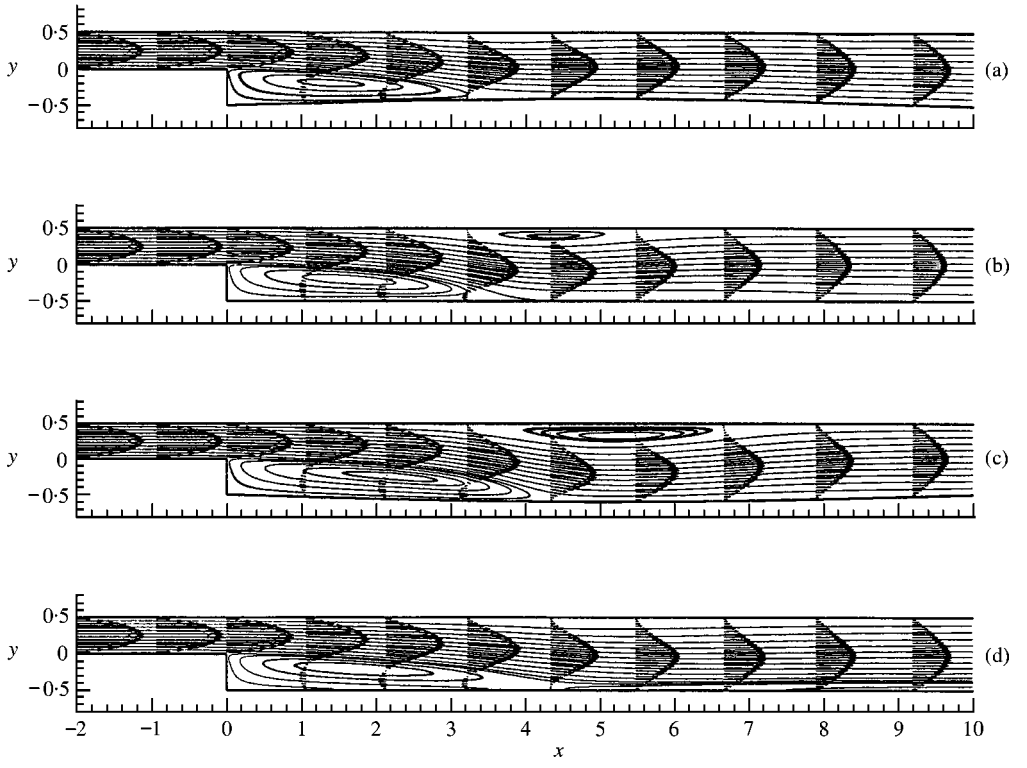

Figure 7. Unsteady flow over a downstream-facing step with an oscillating floor ($H/h = 2$, Re $= 400$, $\omega = 0{\cdot}05$ and $A = 0{\cdot}1$). Typical cross-channel velocity profiles at various axial locations along the computational domain ($-2 < x < 10$) and streamline contours illustrating the separation regions near the upper and lower walls at four different moments during the oscillatory cycle: (a) after 4·00 oscillation cycles; (b) after 4·25 cycles; (c) after 4·50 cycles; (d) after 4·75 cycles.

appearance/disappearance in time of the upper eddy were obtained by extrapolation from the computed results.

It was found that the upper separation region disappears in this case for almost half of the cycle duration. Interestingly, the time interval during which the upper separation region is present decreases with the increase in the reduced frequency of oscillations. One can also notice that the upper separation point is delayed in time with the increase in the reduced frequency, while the reattachment point is advanced in time, thus decreasing the duration in time during which the upper separation region is present.

A graphical illustration of the computed cross-channel velocity profile at various axial locations along the computational domain ($-2 < x < 30$) is shown in Figures 7 and 8 for Re $= 400$, $\omega = 0{\cdot}05$ ($\beta = 20$) and $A = 0{\cdot}1$, at several moments during the oscillation cycle: (a) after 4·00 oscillation cycles of the oscillating portion of the lower wall, which is identical with the moment defined after 5 oscillation cycles; (b) after 4·25 oscillation cycles; (c) after 4·50 oscillation cycles; (d) after 4·75 oscillation cycles. The streamline contours, indicating the recirculation regions near the lower and the upper walls, are also shown in the background of these figures (no special attention should be given to the spacing between streamlines, which does not represent equal increments in terms of the stream function or flow rate, and was arbitrarily chosen in order to enhance the graphical illustration of the separation regions). In Figure 7 one can notice the variation in time of the recirculation

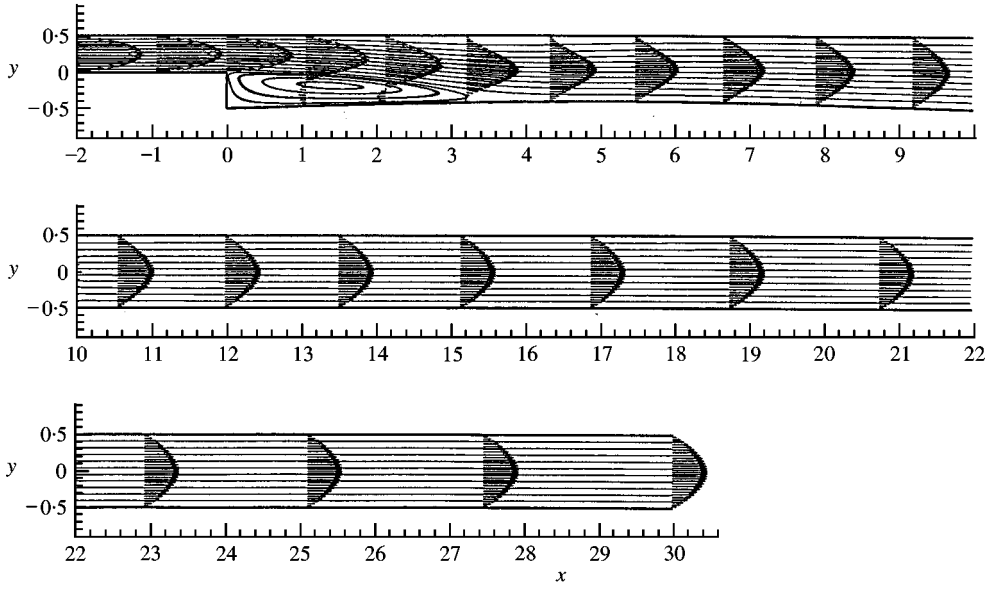

Figure 8. Unsteady flow over a downstream-facing step with an oscillating floor ($H/h = 2$, Re $= 400$, $\omega = 0{\cdot}05$ and $A = 0{\cdot}1$). Typical cross-channel velocity profiles at various axial locations and streamline contours along the entire computational domain ($-2 < x < 30$) after 4 oscillation cycles.

bubbles near the upper and lower walls, and the complete disappearance of the upper separation region at the moments (a) and (d).

It is interesting to note that the velocity profile becomes parabolic well upstream of the outlet boundary of the computational domain (at $x = l_1 = 30$), as shown in Figure 8, which proves that the length of the computational domain behind the downstream-facing step was adequately chosen. However, the mean flow velocity at the outlet, and hence the outlet flow rate as well, slightly varies in time due to the pumping effect of the lower wall oscillations. For example, in the case defined by Re $= 400$, $\omega = 0{\cdot}05$ ($\beta = 20$) and $A = 0{\cdot}1$, the outlet flow rate varies during the oscillation cycle with respect to the inlet flow rate within 6·4%.

An enlarged graphical representation of the streamline contours is illustrated, for the same moments of the oscillation cycle (a), (b), (c) and (d) of Figure 7, in Figure 9. The evolution in time of the separation regions near the upper and lower walls is clearly shown in this figure, as well as the disappearance of the upper separation region at moments (a) and (d). It is to be noted that the coordinates along and across the channel are represented at different scales in this figure.

6. CONCLUSIONS

A time-accurate integration method using artificial compressibility is presented for the analysis of unsteady viscous flows with oscillating walls displaying multiple separation regions. The method is used to solve the unsteady Navier–Stokes equations in a fixed computational domain obtained via a time-dependent coordinate transformation from the real fluid domain with moving boundaries.

The method was first validated for steady viscous flows past a downstream-facing step by comparison with previous numerical solutions and experimental results. The present solutions for steady flows were found to be in excellent agreement with the previous

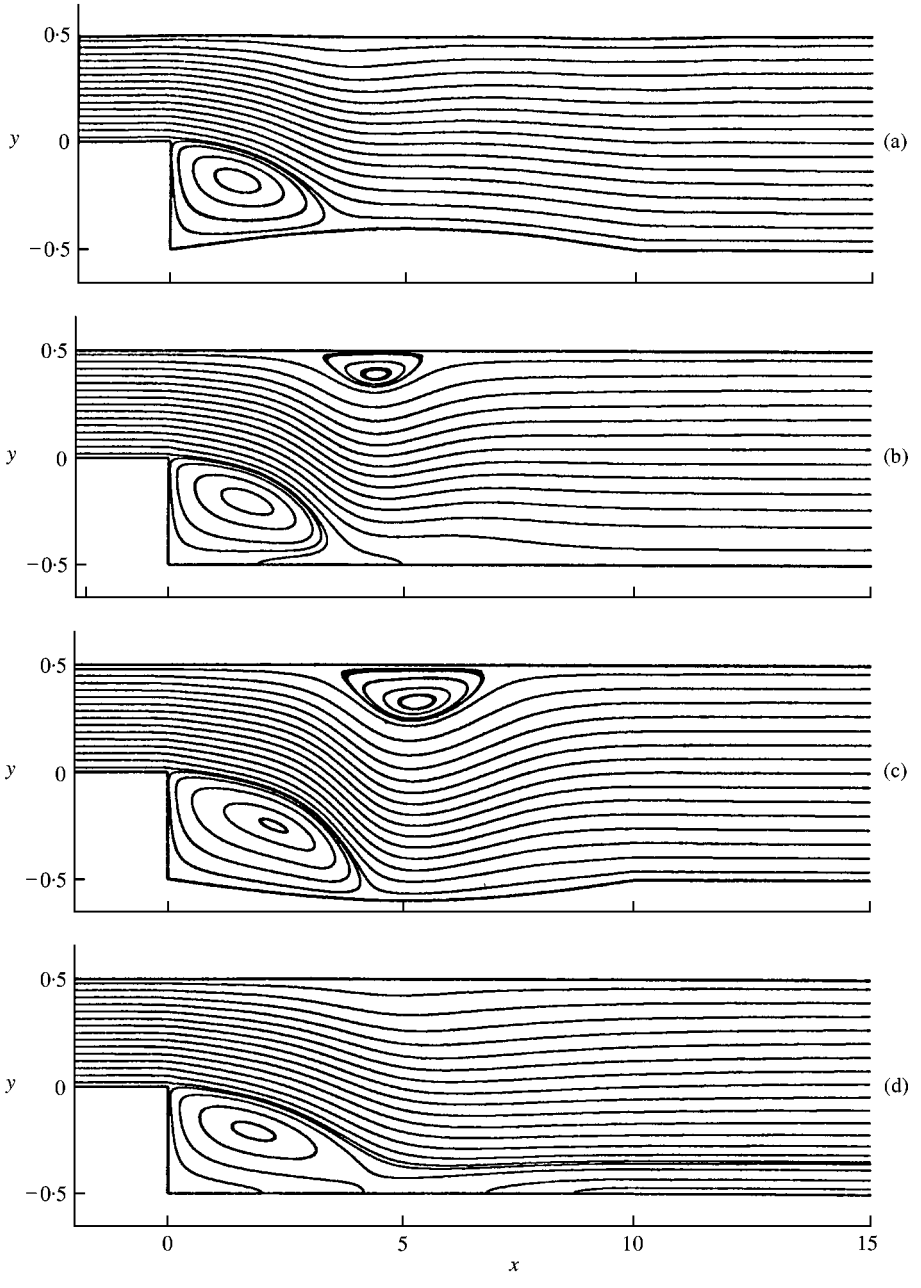

Figure 9. Unsteady flow over a downstream-facing step with an oscillating floor ($H/h = 2$, Re $= 400$, $\omega = 0{\cdot}05$ and $A = 0{\cdot}1$). Enlarged graphical illustration of the streamline contours showing the evolution in time of the separation regions near the upper and lower walls at four different moments during the oscillatory cycle: (a) after 4·00 oscillation cycles; (b) after 4·25 cycles; (c) after 4·50 cycles; (d) after 4·75 cycles. The disappearance of the upper separation region at moments (a) and (d) is clearly shown in this figure.

numerical results, and in good agreement with the experimental results for Reynolds numbers smaller than 600. Larger differences with respect to the experimental results were found for larger Reynolds numbers, due to three-dimensional effects present in the experimental flows.

The method was then used to obtain solutions for the unsteady viscous flows over a downstream-facing step followed by an oscillating floor, for which there are no previously known solutions. This type of unsteady flow is characterized by the presence of a separation region near the lower wall, as well as of another separation region near the upper wall. The locations of the separation and reattachment points on the lower and upper walls were found to vary in time, as expected, due to the lower wall oscillations. The present solutions show the influence of Reynolds number, oscillation amplitude, and reduced frequency (or the oscillatory Reynolds number) on the variation in time of the separation and reattachment locations.

Interestingly, it was found that for Reynolds numbers smaller than 600 the upper separation region is present only for a portion of the oscillation cycle, and simply disappears for the rest of the cycle. It was also found that the maximum length of the upper separation region during the oscillation cycle, and to some extent that of the lower one, increases substantially with the Reynolds number and with the amplitude of oscillations. The time interval during which the upper separation is present decreases with the increase in the oscillation frequency, the upper separation being delayed in time by the frequency increase, while the upper reattachment is advanced in time.

The present unsteady flow solutions, which are obtained for the first time, may be used for the validation of future computational solutions and experimental results as benchmark problems for unsteady flows with multiple separation regions and oscillating boundaries.

References

Abbott, D. E. & Kline, S. J. 1962 Experimental investigations of subsonic turbulent flow over single an double backward-facing step. *ASME Journal of Basic Engineering* **84,** 317–325.

Armaly, B. F., Durst, F., Pereira, J. C. F. & Schonung, B. 1983 Experimental and theoretical investigation of backward-facing step flow. *Journal of Fluid Mechanics* **127,** 1026–1033.

Chen, S. S., Wambsganss, M. W. & Jendrzejczyk, J. A. 1976 Added mass and dumping of a vibrating rod in a confined viscous fluid. *Journal of Applied Mechanics* **43,** 325–329.

Gartling, D. K. 1990 A test problem for outflow boundary conditions — Flow over a backward-facing step. *International Journal for Numerical Methods in Fluids* **11,** 953–967.

Goldstein, R. J., Eriksen, V. L., Olson, R. M. & Eckert, E. R. G. 1970 Laminar separation, reattachment and transition of the flow over a downstream-facing step. *ASME Journal of Basic Engineering* **92,** 732–741.

Inada, F. & Hayama, S. 1990 A study on leakage-flow-induced vibrations. *Journal of Fluids and Structures* **4,** 395–412 and 413–428.

Kim, J. & Moin, P. 1985 Application of a fractional-step method to incompressible Navier–Stokes equations. *Journal of Computational Physics* **59,** 308–323.

Lee, T. & Mateescu, D. 1998 Experimental and numerical investigations of 2-D backward-facing step flow. *Journal of Fluids and Structures* **12,** 703–716.

Mateescu, D. & Païdoussis, M. P. 1985 The unsteady potential flow in an axially-variable annulus and its effect on the dynamics of the oscillating rigid center-body. *ASME Journal of Fluids Engineering* **107,** 615–628.

Mateescu, D. & Païdoussis, M. P. 1987 Unsteady viscous effects on the annular-flow-induced instabilities of a rigid cylindrical body in a narrow annular duct. *Journal of Fluids and Structures* **1,** 197–215.

Mateescu, D., Païdoussis, M. P. & Bélanger, F. 1988 Unsteady pressure measurements on an oscillating cylinder in narrow annular flow. *Journal of Fluids and Structures* **2,** 615–628.

Mateescu, D., Païdoussis, M. P. & Bélanger, F. 1989 A theoretical model compared with experiments for the unsteady pressure on an cylinder oscillating in turbulent annular flow. *Journal of Sound and Vibration* **135,** 487–498.

Mateescu, D., Païdoussis, M. P. & Bélanger, F. 1994a A time-integration method using artificial compressibility for unsteady viscous flows. *Journal of Sound and Vibration* **177,** 197–205.

MATEESCU, D., PAÏDOUSSIS, M. P. & BÉLANGER, F. 1994b Unsteady annular viscous flows between oscillating cylinders. Part I: Computational solutions based on a time integration method. & Part II: A hybrid time-integration solution based on azimuthal Fourier expansions for configurations with annular backsteps. *Journal of Fluids and Structures* **8,** 489–507 and 509–527.

MATEESCU, D., PAÏDOUSSIS, M. P. & SIM, W.-G. 1994c A spectral collocation method for confined unsteady flows with oscillating boundaries. *Journal of Fluids and Structures* **8,** 157–181.

MATEESCU, D., POTTIER, T., PEROTIN, L. & GRANGER, S. 1995 Three-dimensional unsteady flows between oscillating eccentric cylinders by an enhanced hybrid spectral method. *Journal of Fluids and Structures* **9,** 671–695.

MATEESCU, D., MEKANIK, A. & PAÏDOUSSIS, M. P. 1996 Analysis of 2-D and 3-D unsteady annular flows with oscillating boundaries based on a time-dependent coordinate transformation. *Journal of Fluids and Structures* **10,** 57–77.

SOHN, J. L. 1988 Evaluation of FIDAP on some classical laminar and turbulent benchmarks. *International Journal for Numerical Methods in Fluids* **8,** 1469–1490.